Corrosion Mechanism of Plasma-Sprayed Fe-Based Amorphous Coatings with High Corrosion Resistance

Zhenhua Chu[1,2] · **Wenxing Deng**[1] · **Xingwei Zheng**[1] · **Yuyun Zhou**[1] ·
Chunyue Zhang[2] · **Jingxiang Xu**[1] · **Li Gao**[1]

Abstract $Fe_{45}Cr_{16}Mo_{16}C_{18}B_5$ amorphous coatings were deposited on the mild steel substrate (0.45 wt.% C) by plasma spraying, and their corrosion resistance in 3.5 wt.% NaCl solution was compared with those of the substrate and 316 stainless steel. Potentiodynamic tests revealed that the as-prepared coatings had higher resistance to local corrosion than 316 stainless steel due to their wide passivation range. Electrochemical impedance spectroscopy (EIS) measurements further explained the long-term corrosion process of the coatings and indicated their excellent corrosion resistance. Based on this analysis, a schematic diagram of the corrosion mechanism of the coatings was proposed. The obtained results imply that $Fe_{45}Cr_{16}Mo_{16}C_{18}B_5$ amorphous coatings have a promising prospect for industrial applications.

Keywords amorphous alloy · coating · corrosion resistance · electrochemical impedance spectroscopy · plasma spraying

Introduction

Bulk amorphous alloys are rarely used in the engineering field due to their limited glass-forming ability (GFA) (Ref 1). Therefore, amorphous metallic glassy coatings with the same properties of amorphous alloys are generally prepared by thermal spraying to widen the applications of amorphous materials. Different thermal spray techniques, such as plasma, flame, and high-velocity oxygen fuel spraying, are often employed to fabricate amorphous coatings (Ref 2–6).

Among all amorphous coatings, iron-based amorphous alloys have attracted considerable attention due to their high hardness, outstanding wear and corrosion resistance, and low cost (Ref 7–10). Farmer (Ref 10, 11) reported that FeCrMnMoWBCSi coatings fabricated by plasma spraying had higher corrosion resistance than nickel-based coatings in the salt-fog environment. Zhang (Ref 12) found that FeCrMoCYB coatings produced by HVOF with fine powder had a denser structure and poor corrosion resistance than the coatings produced with coarse powder.

Therefore, this study dealt with the characterization of the long-term corrosion behavior and corrosion mechanism of Fe-based amorphous coatings. The corrosion mechanism of the investigated coatings immersed in 3.5 wt.% NaCl solution for 472 h was studied in detail.

Experimental Procedure

$Fe_{45}Cr_{16}Mo_{16}C_{18}B_5$ amorphous powders with the particle size of 16–54 μm were produced by gas atomization, and subsequently, $Fe_{45}Cr_{16}Mo_{16}C_{18}B_5$ amorphous coatings were fabricated by plasma spraying. Plasma spraying is an appropriate method to fabricate amorphous coatings due to

✉ Zhenhua Chu
zhenhua_chu@163.com

✉ Xingwei Zheng
xwzheng@shou.edu.cn

1 Department of Mechanical Engineering, College of Engineering, Shanghai Ocean University, Shanghai 201306, China

2 School of Materials Science and Engineering, Hebei University of Technology, Tianjin 300132, China

its high heating temperature, fast heating rate, and relatively fast cooling rate. The coatings were fabricated by an 80 kW GP-80 plasma-spraying system consisting of a GP-50B control cabinet and a BT-G3 gun. Mild steel plates (0.45 wt.% C) of 12 mm × 10 mm × 10 mm size were selected as the substrate. Before the spraying process, the substrates were sand-blasted to improve the composition of the coatings, and subsequently, adhesive layers of Ni/Al powder were sprayed of the coatings. Table 1 provides parameters of the plasma-spraying process.

The microstructures of the investigated amorphous powders and coatings were studied by scanning electron microscopy (SEM; Hitachi S-4800, Japan) coupled with an EDS system. Ten SEM morphologies for each sample were used to test the porosity of the coatings. The porosity of the coatings was calculated by Image Pro-Plus 6.0 software. The chemical elements of the coatings were revealed by x-ray diffraction (XRD).

The corrosion performances of different samples in 3.5 wt.% NaCl solution were evaluated by a Gamry Interface 1000 electrochemical workstation. All of the electrochemical measurements were conducted at room temperature in a three-electrode cell in which the saturated calomel electrode (SCE) and the graphite electrode acted as the reference and auxiliary electrodes, respectively. Prior to electrochemical tests, all of the specimens were polished. Potentiodynamic polarization curves were recorded at a potential sweep rate of 1 mV s^{-1} after 1 h of immersion at room temperature (when the open-circuit potential (OCP) became stable). Electrochemical impedance spectroscopy (EIS) was conducted at the OCP for 472 h in the frequency range of 100–0.01 Hz, with a sinusoidal amplitude of 10 mV. Impedance plots were interpreted on the basis of equivalent circuits using a suitable fitting procedure by Echem Analyst. The corroded surfaces of the specimens were observed by SEM and XRD after potentiodynamic polarization and EIS tests.

Results

Structures and Morphologies of Amorphous Coatings

The micrograph of feedstock powders prepared by gas atomization is displayed in Fig. 1(a), and it is evident that the powders were composed of smooth spherical particles of size 16–54 μm and had good fluidity during plasma spraying. The XRD patterns of feedstock powders and the Fe-based amorphous coating are presented in Fig. 1(b). The coating exhibited a broad diffraction peak at $2\theta = 44°$, and the absence of obvious crystal peaks indicates that an amorphous structure was successfully formed by plasma spraying. Figure 1 (c and d) reveals the micrographs of the as-sprayed and polished surfaces of the coating. The surface was generally homogeneous. However, due to the formation of pores and flaws, the porosity of the coating reached 1.24%.

Potentiodynamic Polarization Measurements

Figure 2 compares the potentiodynamic polarization plots of the coatings, the carbon steel substrate, and 316 stainless steel in 3.5 wt.% NaCl solution. Potentiodynamic polarization curves of the coatings and stainless steel experienced spontaneous passivation with high corrosion potential, and it implies that they had good corrosion resistance. Iron oxide was first formed in the coatings and improved the corrosion resistance. However, iron oxide is unstable; thus, it dissolved easily in the solution and formed $Cr_2O_3 \bullet Cr_2O_3$ has high corrosion resistance; hence, the passivation phenomenon was observed in the polarization curve of Fe-based amorphous coatings. On the contrary, the passivation phenomenon was not observed in the substrate. Table 2 summarizes important electrochemical parameters (corrosion potential (E_{corr}), corrosion current density (I_{corr}), passivation current density (i_{pass}), transpassive potential (E_{tr}), and corrosion rate) extracted from the polarization plots. Although stainless steel had the best corrosion potential (− 254 mV) and the lowest corrosion current density (1.10×10^{-7} A cm^{-2}), its pitting potential was low (only about 0.3 V). In contrast, the passivation region of amorphous coatings was wider than

Table 1 Detailed parameters of the coatings produced by plasma spraying

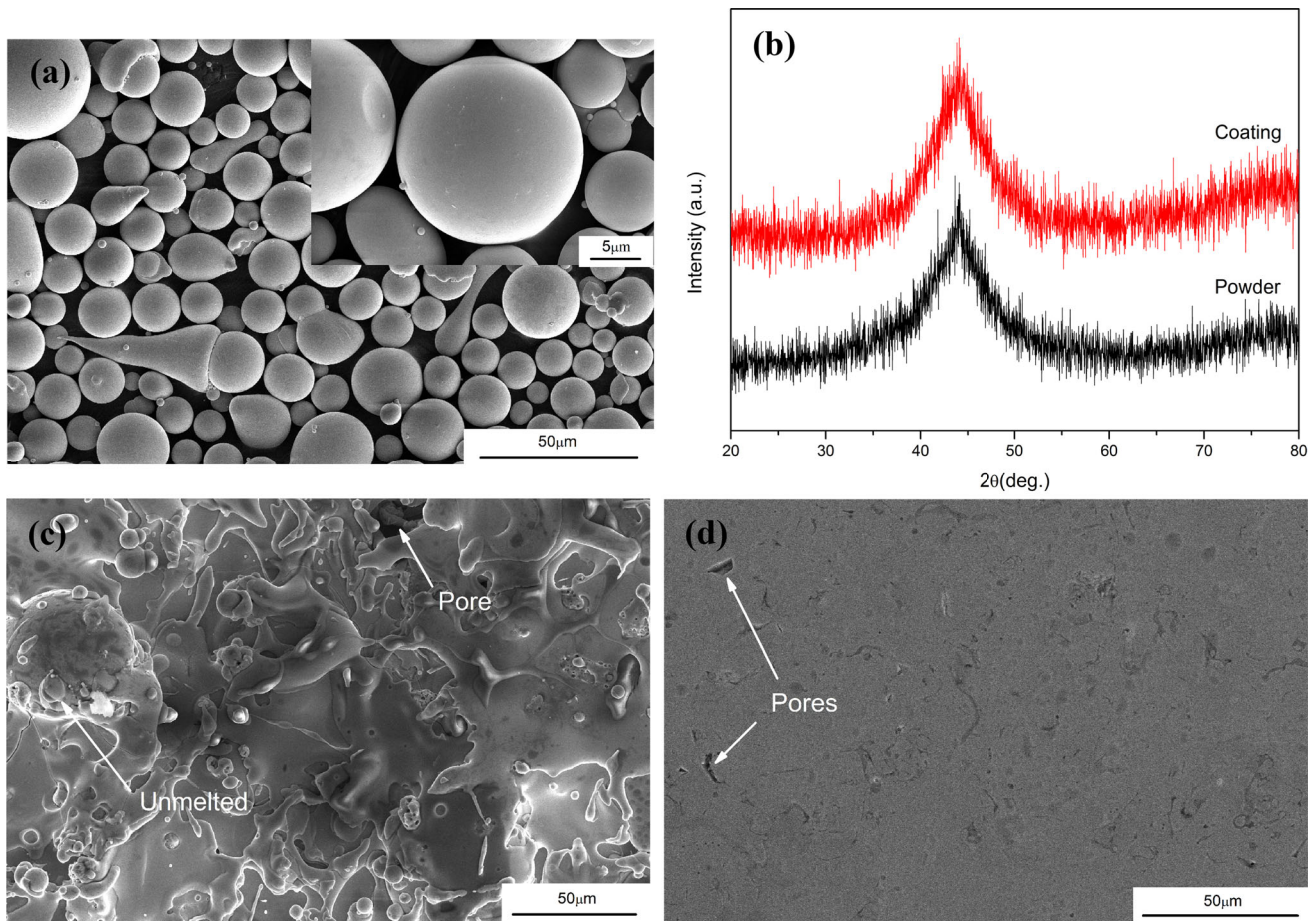| Spray parameters	Adhesive coating	Fe-based amorphous coating
Voltage, V	60	70
Current, A	500	500
Spray distance, mm	100–120	100
Primary gas (Ar) flow rate, Lmin^{-1}	80	70–80
Secondary gas (H$_2$) flow rate, Lmin^{-1}	20	20

Fig. 1 (a) SEM micrograph of the as-atomized $Fe_{45}Cr_{16}Mo_{16}C_{18}B_5$ powders; (b) XRD patterns of the feedstock powders and plasma-sprayed coating; (c) SEM micrographs of as-sprayed surface and polished surface (d)
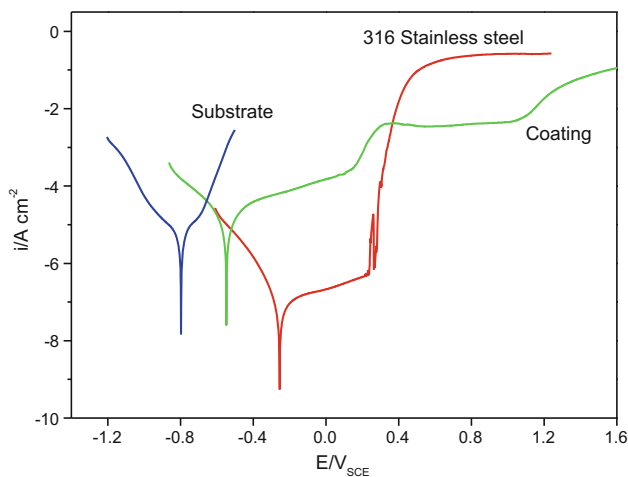

Fig. 2 Polarization curves of coating compared with the substrate and 316 stainless steel in 3.5 wt.% NaCl solution

that of stainless steel although the corrosion potential of amorphous coatings was slightly lower than that of stainless steel. When the potential reached 1058 mV, the corrosion current density increased significantly; it indicates that the passive film or the coating was gradually destroyed.

The corroded surfaces of different samples after potentiodynamic polarization are presented in Fig. 3. Severe corrosion damage occurred on the substrate, and its surface was covered with corrosion products and pits. The corroded surface morphology of the substrate is displayed in Fig. 3(a). In the Fe-based coating, only a few small corrosion pits were distributed around the defects (Fig. 3b). About 316 stainless steel still retained the metal surface; however, some large corrosion pits (length up to 0.6 mm) appeared on the local surface (Fig. 3c). Moreover, some crystalline NaCl still remained on its surface. Therefore, it can be inferred that the coating had the best corrosion resistance. In addition, the corrosion rate of the amorphous coating (0.28 mm a^{-1}) was about 66% lower than that of the substrate.

Table 2 Summary of the electrochemical parameters of different samples

Sample	E_{corr}, mV	i_{corr}, A cm^{-2}	i_{pass}, A cm^{-2}	E_{tr}, mV	Corrosion rate, mm a^{-1}
316 stainless steel	− 254	1.10×10^{-7}	2.27×10^{-6}	303	< 0.01
Fe-based coating	− 547	1.24×10^{-5}	4.23×10^{-3}	1058	0.144
45 steel	− 733	4.87×10^{-4}	…	…	0.703
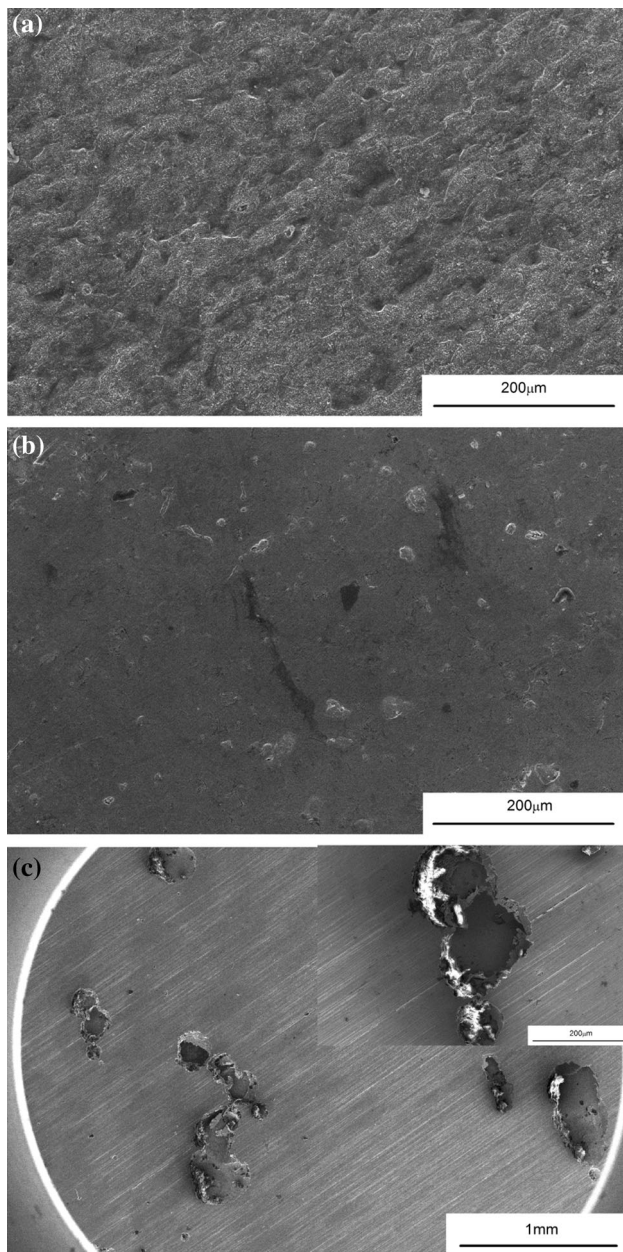
Fig. 3 SEM images of the corroded surface of different samples after potentiodynamic polarization testing: (a) substrate; (b) Fe-based amorphous coating; (c) 316 stainless steel

EIS Measurements and Equivalent Circuit Models

The EIS curves of different samples are presented in Fig. 4. After 4 h of immersion, only one large capacitive loop was formed in the Nyquist plot (Fig. 4a), and it corresponds to only one peak in the Bode phase plot in Fig. 4(b). Therefore, the formation of a shielding layer on the amorphous coating effectively blocked the corrosive medium from reaching the coating/substrate interface. This phenomenon can be attributed to the penetration of the electrolyte into the coating through defects, leading to the spontaneous passivation of the coating and the formation of a dense passivation film. When the immersion time increased to 24 h, a second peak appeared in the low-frequency region of the Bode phase plot and the phase angle shifted toward the left. Simultaneously, the Nyquist plot exhibited two consecutive semicircles, reflecting the existence of two time constants. The time constant corresponding to the high-frequency end-capacitance arc appeared from the contribution of the capacitance of the amorphous coating to the micropore resistance of the coating surface, whereas the time constant corresponding to the low-frequency end-capacitance arc originated from the double electric layer capacitance and the polarization resistance. This phenomenon indicates that the electrolyte effectively penetrated the substrate (Ref 13). Once the corrosive solution penetrated the substrate, an electric double-layer capacitor was formed between the electrolyte and the coating/substrate, resulting in further electrochemical reactions. However, when the immersion time exceeded 120 h, the low-frequency capacitive arc in the Nyquist graph disappeared. The small capacitive arc overlapped with the large capacitive arc; thus, it was difficult to distinguish the two time constants. It happened because the accumulation of corrosion products blocked the corrosive fluid pathway. As the corrosion time increased, the impedance value fluctuated within a small range. Corrosion products had a "blocking effect" on gaps and holes of the coating; thereby, the accumulation and dissolution of corrosion products caused a change of the impedance value. When the immersion time reached 472 h, the coating did not rupture due to its excellent corrosion resistance.

According to the above analysis, equivalent circuits were plotted to describe the reaction process of the
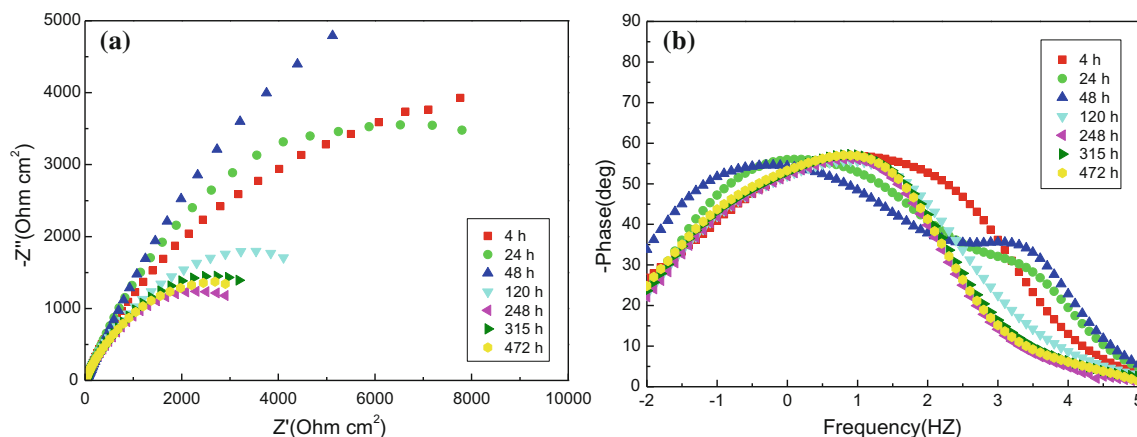
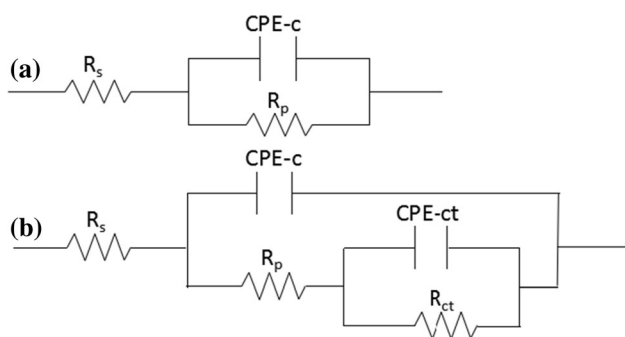Fig. 4 The Nyquist (a) and Bode phase plots (b) of amorphous coating, respectively

Fig. 5 Equivalent circuits for describing the impedance behavior of amorphous coating: (a) during earlier immersion stage; (b) during later immersion stage

amorphous coating during different stages of corrosion (Fig. 5). The equivalent circuit was applied to describe the reaction mechanism of initial corrosion. The equivalent circuit in Fig. 5a is composed of the solution resistance (R_s), the pore resistance (R_p) produced by the formation of the ionic conduction path through the coating, and the constant phase element (CPE-c). The circuit in Fig. 5(b) has more than two elements: CPE-ct (double-layer capacitance between the electrolyte and the coating/substrate) and R_{ct} (charge transfer resistance of the coating/steel interface). This circuit is suitable to describe the mechanism of medium period (Ref 14). Figure 6 exhibits the changes in electrochemical parameters obtained from the equivalent circuit. The Rp value of the coating reached 1.14×10^4 Ω cm^2 due to the formation of a dense passivation film after 4 h of immersion. The Rp value decreased to 38 Ω cm^2 after 24 h of immersion due to the destruction of the passivation film by corrosive ions (Ref 15). The Rp value increased to 57 Ω cm^2 after 48 h of immersion. When the solution permeated the pore area, the adhesive oxide films of Cr and Mo were formed and hindered the solution infiltration. With the continuous penetration of NaCl solution, the capacitance of the coating

gradually increased; it indicates that the protective ability of the coating was gradually weakened. In addition, the value increased gradually with the immersion time. The small fluctuation in the CPE-c value implies the formation and redissolution of corrosion products. When the immersion time reached 472 h, the R_{ct} value decreased to ~ 1 $K\Omega$ cm^2. The permeation of chloride ions destructed the close bonding between the substrate and the coating, resulting in the failure and peeling of the coating. With the continuous infiltration of NaCl solution, the corrosion resistance of the coating decreased and the coating capacitance increased; thus, the protective ability of the Fe-based amorphous coating decreased gradually. Subsequently, corrosion products were formed after 472 h of immersion (Fig. 7a). Corrosion products were mainly composed of hydroxyl iron oxide, a small amount of Fe_3O_4 and NaCl residue, and chromium-molybdenum oxide. Figure 7b reveals that the surface of the coating mainly consisted of iron oxide and NaCl residue.

Discussion

On the basis of the above-discussed analysis, the long-time corrosion mechanism of $Fe_{45}Cr_{16}Mo_{16}C_{18}B_5$ amorphous coatings was proposed. The long-range disorder in the microstructures of the investigated amorphous coatings implies that grain boundaries could not improve their corrosion resistance; therefore, the impacts of chemical elements on their corrosion resistance should be discussed. Figure 8 describes the corrosion process of these coatings in 3.5 wt.% NaCl solution. Numerous micro-defects, such as micropores and flaws, appeared on the surfaces and interfaces of the coatings due to the formation of partial oxides and the solidification of semi-molten particles during thermal spraying (Fig. 8a) (Ref 15, 16). When the sample was immersed in NaCl solution, pores on the
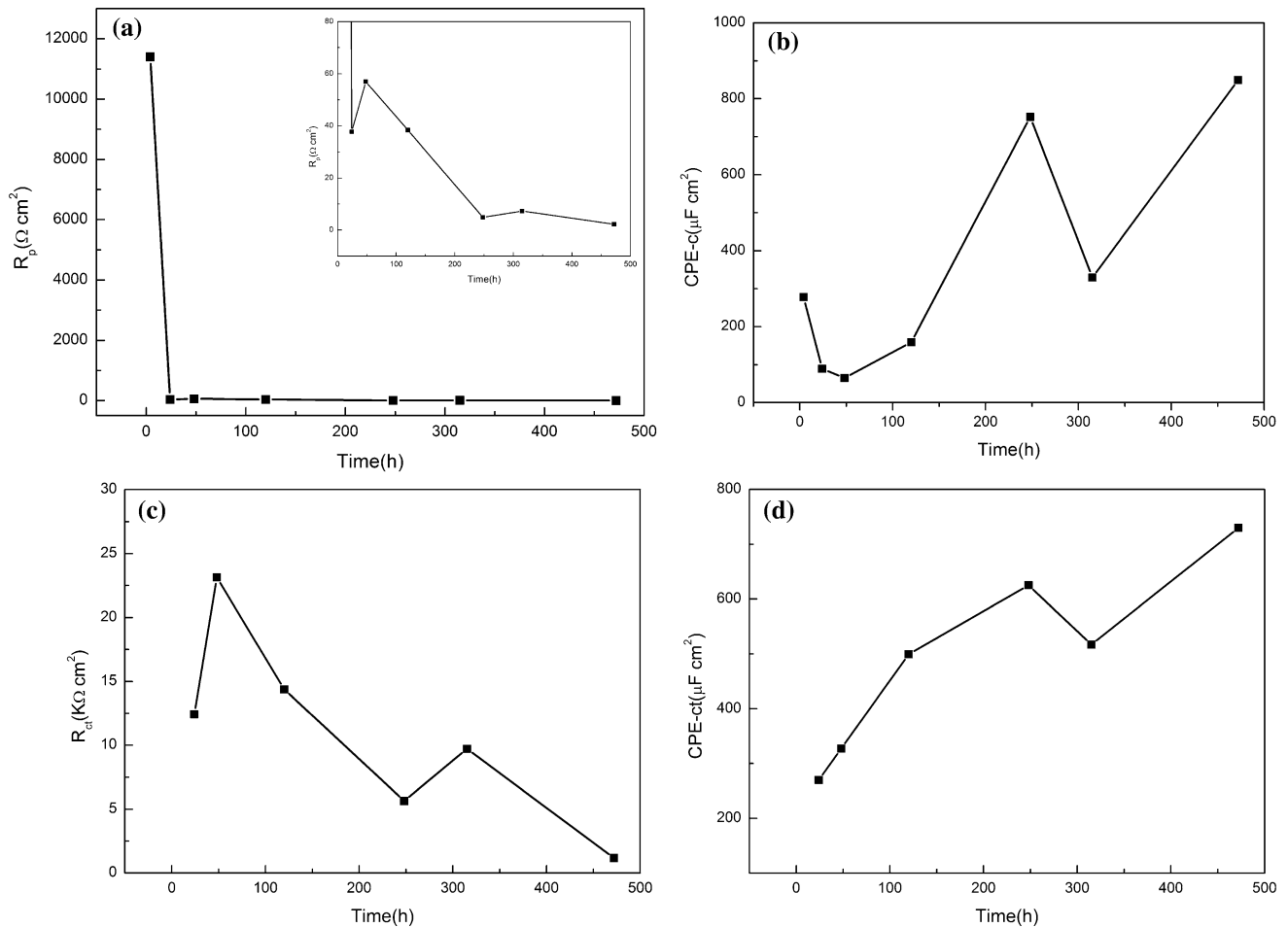
Fig. 6 Relationship between equivalence elements of amorphous coating and corrosion times: (a) R_p–time curve; (b) CPE-c–time curve; (c) R_{ct}–time curve; (d) CPE-ct–time curve
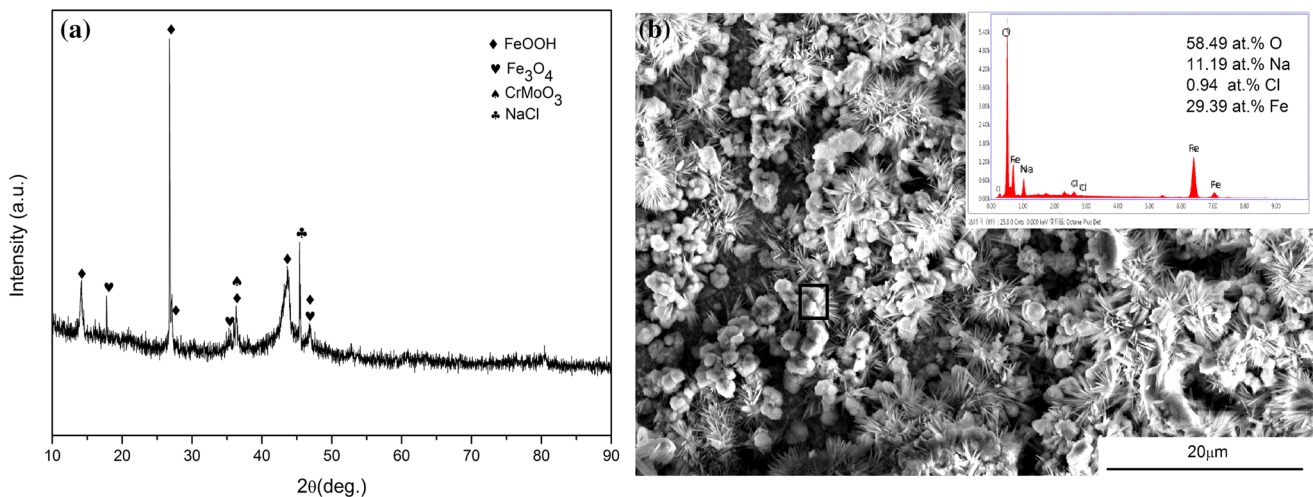

Fig. 7 Chemical analysis of the corrosion products: (a) XRD pattern analysis; (b) SEM image and the EDS result

coating surface became filled with the corrosive media (Fig. 8b). As the coating contained Cr and Mo, Cr_2O_3 was easily formed as a protective passivation film. Moreover, the presence of Mo promoted the formation of the adhesive passive coating and slowed down the dissolution of Cr (Ref 17–19). With the increase in the immersion time, chloride
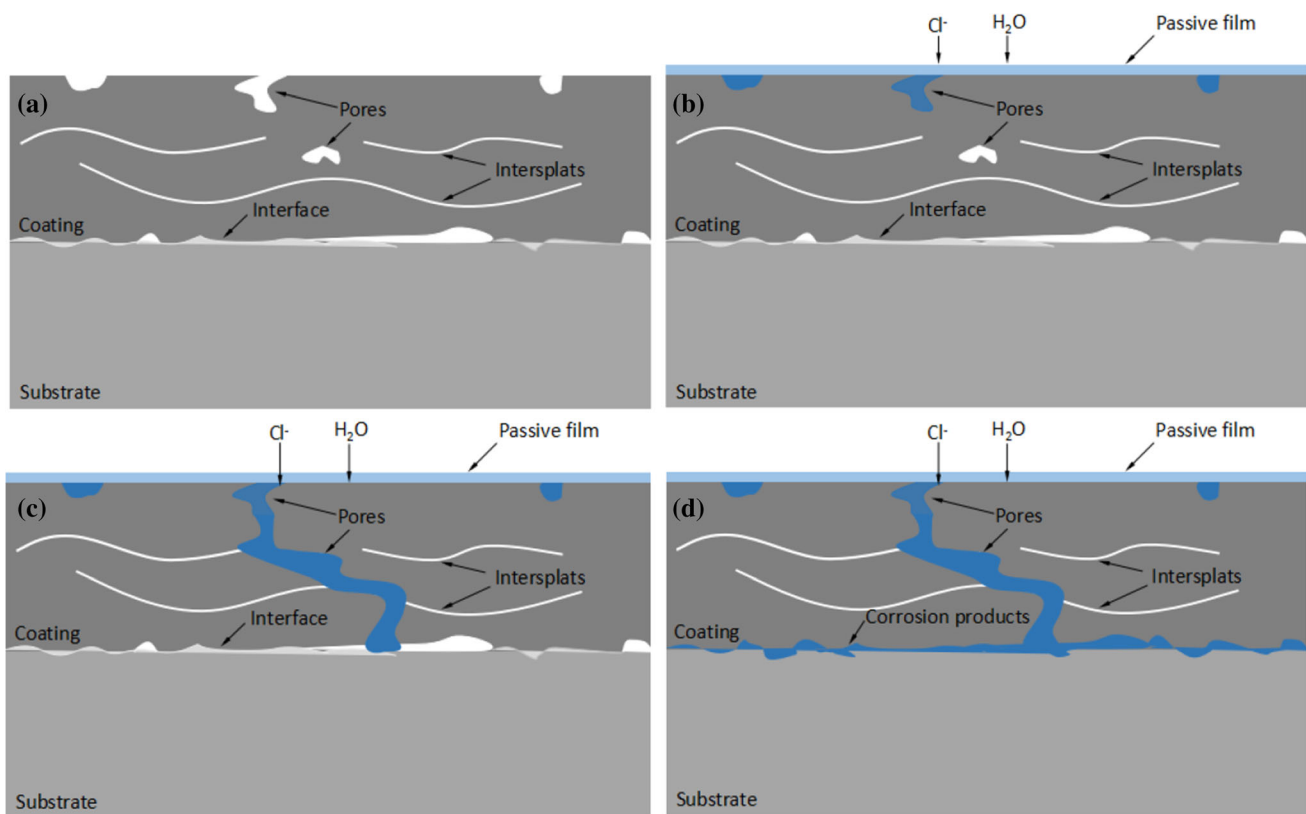
Fig. 8 The mechanism of the corrosion process

ions permeated the coating through pores and intersplats and then reached the coating/substrate interface. As the substrate acted as the anode, electrochemical reactions promoted the formation of corrosion products and generated local interface bubbles (Fig. 8c). Figure 8d reveals that the interface was eventually covered with corrosion products, leading to coating failure and peeling off. Therefore, the presence of pores in the coating significantly reduced the corrosion resistance and accelerated its failure.

Conclusions

Fe45Cr16Mo16C18B5 coatings with a glassy structure were successfully prepared by plasma spraying. In comparison with the substrate and 316 stainless steel, the as-prepared coatings had better resistance to local corrosion. Moreover, these Fe-based coatings had a high passivation film breakdown potential ($\sim$ 1.2 V) and small corrosion damage. EIS spectra revealed that the long-term corrosion process of these coatings could be divided into two stages. The fluctuation of the time constant could be attributed to the passivation film, porosity, and the "plugging effect" of the corrosion products. After 472 h of long-term immersion, porous and loose corrosion products were mainly composed of hydroxyl iron oxide.

References

1. A. Kobayashi, S. Yano, H. Kimura, and A. Inoue, Mechanical Property of Fe-Base Metallic Glass Coating Formed by Gas Tunnel Type Plasma Spraying, *Surf. Coat. Technol.*, 2008, **202**, p 2513-2518
2. A. Inoue, X.M. Wang, and W. Zhang, Development and Applications of Bulk Metallic Glasses, *Rev. Adv. Mater. Sci.*, 2008, **18**, p 1-9
3. Z. Zhou, L. Wang et al., Formation and corrosion behavior of Fe-based amorphous metallic coatings by HVOF thermal spraying, *Surf. Coat. Technol.*, 2009, **204**, p 563-570
4. J. Blink, J. Farmer et al., Applications in the Nuclear Industry for Thermal Spray Amorphous Metal and Ceramic Coatings, *Metall. Mater. Trans. A*, 2009, **40**, p 1344-1354
5. B. Shen, A. Inoue, and C. Chang, Superhigh strength and good soft-magnetic properties of (Fe, Co)–B–Si–Nb bulk glassy alloys with high glass-forming ability, *Acta Mater.*, 2004, **52**, p 4093-4099
6. D.J. Branagan and M. Breitsameter, High-performance nanoscale composite coatings for boiler applications, *J. Therm. Spray Technol.*, 2005, **14**, p 196-204

7. J. Voyer, Wear-Resistant Amorphous Iron-Based Flame-Sprayed Coatings, *J. Them. Spray Technol.*, 2010, **19**, p 1013-1023

8. X.Q. Liu, Y.G. Zheng et al., Microstructure and Properties of Fe-Based Amorphous Metallic Coating Produced by High Velocity Axial Plasma Spraying, *J. Alloys Compd.*, 2009, **484**, p 300-307

9. J. Farmer, S. Cheng et al., Iron-Based Amorphous-Metals: High-Performance Corrosion-Resistant Materials (HPCRM) Development Final Report, *Metall. Mater. Trans. A*, 2009, **40**, p 1289-1305

10. J. Farmer, S.D. Day et al., Terahertz Polaritonics, *J. Mater. Res.*, 2007, **22**, p 2291-2311

11. S. Kumar, C. Lee et al., Phase Dependence of Fe-Based Bulk Metallic Glasses on Properties of Thermal Spray Coatings, *J. Alloys Compd.*, 2009, **475**, p 9-12

12. C. Zhang, R.Q. Guo et al., Influence of the Size of Spraying Powders on the Microstructure and Corrosion Resistance of Fe-Based Amorphous Coating, *Electrochim. Acta*, 2011, **56**, p 6380-6388

13. Y. Yang, C. Zhang et al., Effects of Crystallization on the Corrosion Resistance of Fe-Based Amorphous Coatings, *Corros. Sci.*, 2012, **59**, p 10-19

14. S.D. Zhang, J. Wu, W.B. Qi et al., Effect of Porosity Defects on the Long-Term Corrosion Behaviour of Fe-Based Amorphous Alloy Coated Mild Steel, *Corros. Sci.*, 2016, **110**, p 57-70

15. J.M. Guilemany, N. Espallargas et al., Influence of Spraying Parameters on the Electrochemical Behaviour of HVOF Thermally Sprayed Stainless Steel Coatings in 3.4% NaCl, *Surf. Coat. Technol.*, 2006, **200**, p 3064-3072

16. J. Saaedi, T.W. Coyle et al., Effects of HVOF Process Parameters on the Properties of Ni-Cr Coatings, *J. Therm. Spray Technol.*, 2010, **19**, p 521-530

17. J. Kawakita and S. Kuroda, Corrosion Resistance of HVOF Sprayed HastelloyC Nickel Base Alloy in Seawater, *Corros. Sci.*, 2005, **47**, p 2053-2062

18. M. Naka, K. Hashimoto, and T. Masumoto, Effect of Addition of Chromium and Molybdenum on the Corrosion Behavior of Amorphous Fe-20B, Co-20B and Ni-20B Alloys, *J. Non-Cryst. Solids J.*, 1979, **34**, p 257-266

19. D. Yang, C. Liu et al., Corrosion Behavior of Plasma Sprayed Ceramic and Metallic Coatings on Carbon Steel in Simulated Seawater, *Mater. Des.*, 2013, **52**, p 630-637